Hochschule München University of Applied Sciences

Characterization of Humidity-Sensors based on Polymer Sensing Layer

Master Thesis

to obtain the academic degree Master of Science (M.Sc.) at the university of applied sciences and mechatronics in Munich

by

Syed Fahad Ali

(Born 18/11/1996 in Karachi, Pakistan)

31 August 2022

Department of Applied Sciences and Mechatronics

Micro- and Nanotechnology

Matriculation nr:	03091019
Email:	s.ali@hm.edu
Faculty:	Applied sciences and mechatronics
Course of study:	Micro- and Nanotechnology
Internal Supervisors:	Prof. Dr. Ullrich Menczigar at the FH Munich
	Prof. Dr. Alfred Kersch at the FH Munich
External Supervisors:	Ph.D. Dominik Udiljak at the Infineon Technologies AG
	Dr. Jamila Boudaden at the Fraunhofer EMFT

Abstract

In this study various electrical properties of humidity sensors based on polyimide (PI) layer were characterized. The sensors were manufactured at the Fraunhofer Institute for Microsystems and Solid-State Technology (EMFT) as Inter Digital Transducers (IDT) with a polyimide layer. Changes in the electrical properties were due to a change in the permittivity of the PI layer under different environmental conditions. Using Wafer Prober, EMFT sensors were characterized at different temperatures and bias voltages. The capacitance measurements were conducted for a frequency range from 1 kHz to 1 MHz at the Fraunhofer EMFT. Two reference sensors were compared with HAST (Highly Accelerated Stress Test) built-in sensors to monitor humidity and temperature inside the HAST chamber. Afterward, EMFT sensors were tested at 130 °C and 85 % RH inside the HAST chamber.

Keywords: Inter Digital Transducer, Polyimide PI, EMFT sensors, HAST chamber (Highly Accelerated Stress test).

Zusammenfassung

In dieser Masterarbeit verschiedene elektrische Eigenschaften von Feuchtigkeitssensoren auf Basis einer Polyimid (PI)-Schicht wurden charakterisiert. Die Sensoren wurden am Fraunhofer-Institut für Mikrosysteme und Festkörpertechnik (EMFT) als Inter Digitaler Wandler (IDW) mit einer Polyimid-Schicht hergestellt. Änderungen der elektrischen Eigenschaften waren auf eine Änderung der Permittivität der PI-Schicht unter verschiedenen Umgebungsbedingungen zurückzuführen. Unter Verwendung eines Wafer Probers wurden EMFT-Sensoren bei verschiedenen Temperaturen und elektrischen Vorspannungen charakterisiert. Die Kapazitätsmessungen wurden für einen Frequenzbereich von 1 kHz bis 1 MHz an der Fraunhofer EMFT durchgeführt. Referenzsensoren wurden mit eingebauten HAST eingebaute Sensoren (Highly Accelerated Stress Test) verglichen, um Feuchtigkeit und Temperatur in der HAST-Kammer zu überwachen. Danach wurden EMFT-Sensoren bei 130 °C und 85 % RH in der HAST-Kammer getestet.

Schlüsselwörter: Inter Digitaler Wandler, Polyimide PI, EMFT-Sensoren, HAST Kammer (Highly Accelerated Stress Test).

Contents

Abstract III

Zusammenfassung IV

Index of abbreviations VII

List of Figures IX

List of Tables XI

1. Introduction 1

2. Theoretical background 3

2.1 Absolute and relative humidity 3

2.2 Temperature-humidity sensors 4

2.2.1 Resistive temperature sensors 5

2.2.2 Capacitive humidity sensors 6

2.3 Polyimide Sensing Layer 7

2.4 Polarization Mechanisms of PI 8

2.4.1. Electronic polarization 8

2.4.2. Orientation or dipolar polarization 9

2.4.3. Ionic polarization 10

2.4.4. Interfacial polarization 10

3. Methods and Material 11

3.1 EMFT sensor layout 11

3.2 Wafer probe analyzer 12

3.3 Highly Accelerated Stress Test (HAST) System 13

3.4 Reference Temp-Humidity sensors 18

4. Results 22

4.1 Wafer Probe measurements 22

4.2 Reference sensors measurements 27
4.3 HAST system measurements 29
5. Summary & Outlook 30
5.1 Summary 30
5.2 Outlook 31
Bibliography 32
Appendix 36
a. Arduino coding for BME280 sensor 36
b. Arduino coding for HTU31D sensor 37
Declaration of Authorship 39

Index of abbreviations

EMFT	**F**raunhofer Research Institute for **M**icrosystems and Solid-State **T**echnology
IDT	**I**nter **D**igital **T**ransducer
TCR	**T**emperature **C**oefficient of **R**esistance
IDW	**I**nter**D**igitaler **W**alder
PI	**P**oly**i**mide
HAST	**H**ighly **A**ccelerated **S**tress **T**est
AC	**A**lternating **C**urrent
DC	**D**irect **C**urrent
AH	**A**bsolute **H**umidity
RH	**R**elative **H**umidity
DP	**D**ew **P**oint
PCB	**P**rinted **C**ircuit **B**oard
TiW	**T**itanium **T**ungsten
DIP	**D**ual **I**nline **P**ackage
DUT	**D**evice **U**nder **T**est
DFN	**D**ual **F**lat **N**o-lead
LGA	**L**and **G**rid **A**rray
SMU	**S**ource **M**easuring **U**nit

List of Figures

2.1 The carrier diagram represents the relation between RH and AH with respect to temperature. 4
2.2 The schematic view of a resistive temperature sensor consists of a gold film pattern placed on a ceramic base. 5
2.3 Schematic representation of capacitive humidity sensor. 7
2.4 General chemical structure of polyimide (PI) polymer attached with imide-groups. 7
2.5 Image of electronic polarization of atom. 9
2.6. Representation of orientational or dipolar polarization. 9
2.7 Image of ionic polarization. 10
2.8 Visualization of interfacial polarization. 10
3.1 Schematic view of EMFT-Temp-Humidity sensors A and C layout. 11
3.2 Setup of Wafer Probe Analyzer. 12
3.3 Connected EMFT sensors with wafer probes. 12
3.4 Block diagram of the working process of a Wafer Probe analyzer. 13
3.5 The Highly Accelerated Stress Test (HAST) System contains two vessels with a control panel outside terminals to connect the specimen with the external test equipment. 14
3.6 Inner view of the chamber of the HAST system EHS-2221MD. 15
3.7 SMU (Source Measuring Unit) consists of 13 independent voltage sources provide DC voltage up to 30V with 10nA max resolution. 16
3.8 Sensors A and C were glued, wire-bonded to C-DIPs, and connected with Teflon-gold PCB through a mounting hole. 17
3.9 Selected reference sensors HTU31D and BME280 with the same principle as EMFT Temp-Humidity Sensors. 18
3.10 Schematic design of both reference sensors HTU31D and BME280 to place on Teflon-gold PCB inside the HAST chamber. 19
3.11 HTU31 sensor breakout board by Adafruit and BME280 sensor breakout board by Pimoroni respectively. 20

3.12 I^2C interfacing between Arduino microcontroller and reference humidity sensors. 20
3.13 Installed reference sensor with PCB Teflon inside the HAST chamber. 21
4.1 Generic C-f measurements of both humidity sensors at 30 V DC with 250 mV AC amplitude. 22
4.2 Capacitance (C-V) and conductance (G-V) measurements at three different temperatures of both humidity sensors A and C respectively, at a fixed frequency of 1 kHz and in the bias voltage range from -30 V to +30 V DC in 0.3 V steps. 23
4.3 Current and voltage (I-V) characteristics at three different temperatures of both humidity sensors A and C with a limitation of 10 mA and in a bias voltage range from 0 V to +30 V DC in 0.1 V steps. 24
4.4 Current and voltage (I-V) characteristics at three different temperatures of both temperature sensors A and C with a limitation of 10 mA and in a bias voltage range from 0 V to +30 V DC in 10 mV steps. 25
4.5 Resistive behavior of both temperature sensors A and C at heating and cooling temperature. 26
4.6 Comparison of temperature and humidity between BME280 reference sensor and HAST built-in sensors inside the chamber. 27
4.7 Comparison of temperature and humidity between HTU31D reference sensor and HAST built-in sensors inside the chamber. 28
4.8 Microscopic images of EMFT temp-humidity sensors A and C after testing for up to 100 hours at 130 °C temperature with 85 % relative humidity inside the HAST chamber. 29
A. Arduino Uno microcontroller coding for BME280 reference sensor. 36
B. Arduino Uno microcontroller coding for HTU31D reference sensor. 37

List of Tables

3.1 Electrical specifications of SMU (Source Measuring Unit). 15

4.1 Conductance values of both EMFT humidity sensors A and C were extracted from the linear regression slope of each I-V characteristic curve. 25

4.2 Conductance values of both EMFT temperature sensors A and C were extracted from the linear regression slope of each I-V characteristic curve. 26

1. Introduction

Relative humidity (RH) and temperature sensors are always demanding and have many applications in various fields including the medical field and industrial area [1]. Measuring RH has always been challenging due to the lack of stable and reliable sensors. As well as, the cross-sensitivity to temperature and different gases further complicates the calibration procedure of humidity measurements with RH sensors [2].
There are three different common ways to measure RH:

- By Comparing the temperature between a saturated environment and the environment of interest.
- By measuring the change of mechanical properties of a film or filament.
- By measuring the change of electrical properties like capacitance/resistance [3].

This thesis concentrates on RH sensors which measure a change in their electrical properties, especially their capacitance. That reflects the changes in the dielectric function of the Polyimide (PI)-layer which covers the gold electrodes formed as an Inter Digitated Transducer (IDT) in the presence of different RH levels. As the change in the electrical properties is activated by water molecules penetrating the Polyimide (PI)-layer. Therefore, an electric field can be generated between the IDT electrodes with an applied voltage which changes the capacitance. Polyimide (PI) is a heat-resistant polymer which acts as a dielectric capacitor because of its good thermal and mechanical stability [4].
As reliability is defined as the quality of the sensor over time. Therefore, reliability is a time-consuming procedure. So, reliability tests can be carried out under known stress conditions for a specific period to be able to ensure that devices maintain their function throughout their expected lifetime.
The HAST test, which is a Highly Accelerated Stress Test, is an intriguing technique to test the reliability of electronics. It evaluates the humidity resistance of samples at different humidity and temperature values. Its objective is to evaluate a test specimen's moisture resistance by raising the water vapor pressure in the test chamber to high level than the partial water vapor pressure within the test specimen. This method temporarily increases moisture entry into the sample. The test is carried out at a predetermined temperature, relative humidity, or pressure. In a state of water vapor

pressurization, the atmosphere generally has a temperature of at least 100°C. When pressure is considered as an environmental component, HAST is sometimes characterized as a combined test. HAST comes in saturated and unsaturated forms. The former is commonly performed at 121°C and 100% RH, whereas the latter is performed at 110, 120, or 130°C and 85% RH. Unsaturated tests are typically performed on electrical components. HAST is a pretty extreme test, with an acceleration factor ranging from tens to hundreds of times under 85°C and 85% conditions. Because of the extreme acceleration, it is important to look into failure mechanisms. The main advantage of the HAST is that high-temperature and humidity values can be set inside the HAST chamber, for instance, 130 °C and 85 % RH respectively. Another benefit of the HAST is that the test time can be reduced to 3-4 days rather than weeks for current state-of-the-art reliability tests [5].

By decreasing test duration for reliability tests, companies can achieve a shorter time to market while ensuring their level of quality and reliability.

The main objectives of this thesis are summarized in three parts. The first part is dedicated to the electrical measurements of the Fraunhofer EMFT sensors done in the wafer probe analyzer, including AC response which is a capacitance-frequency curve, DC responses like capacitance-voltage and current-voltage curves as well as resistance measurements concerning different temperature responses.

In the second part, reference sensors with the same principle as EMFT sensors are selected and implemented inside the HAST chamber to trace the differences in relative humidity and temperature values of the reference sensors and the HAST chamber sensors. To set the reference for later calibration.

The third part is based on testing the EMFT temp-humidity sensors inside the HAST chamber for data validation, comparison, and sensor calibration.

2. Theoretical background

2.1. Absolute and Relative Humidity

Relative humidity (RH) is the percentage of water vapor in the saturated air at the same temperature. In other words, it is the ratio of the partial pressure of water vapor (pH_2O) with the mixture of the equilibrium vapor pressure of water (p^*H_2O) as shown in Equation 2.1 [6].

$$\text{Relative humidity} = \emptyset = \frac{pH_2O}{p * H_2O} \qquad Eq: 2.1$$

RH can be increased up to 100 % if the temperature reaches the dew point (DP). The DP is the constant temperature at which air requires to be cool and condensed into water droplets. In other words, RH is the ratio of absolute humidity (AH) present to the maximum possible humidity (RH_{max}) at a given temperature as given in Equation 2.2 below. Mostly the maximum humidity indicates the amount of water at a fixed temperature in a fixed volume [7].

$$RH = \frac{AH}{RH_{max}} x\ 100\ \% \qquad Eq: 2.2$$

On the other side, the exact quantity of water vapor in the air describes the AH, in other words, AH can be calculated with the mass of water vapor (m_{water}) divided by the cubic meter volume of air V_{air} as expressed in Equation 2.3.

$$AH = \frac{m_{water}}{V_{air}} \qquad Eq: 2.3$$

When absolute humidity is constant, relative humidity is directly dependent on temperature exponentially. Due to this fact, it is also important to monitor the temperature of that specific region where humidity sensor will be used. That is why many humidity sensors are also required to measure temperature [8]. A carrier diagram can illustrate all dependencies between each AH and RH. It shows the maximum

humidity as a function of temperature and relative humidity, as can be seen in Figure 2.1.

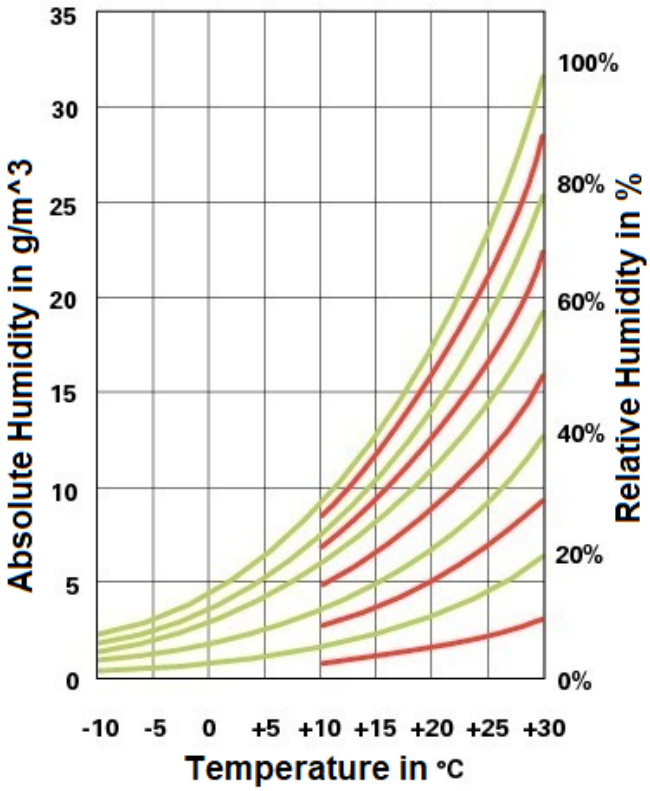

Fig 2.1: The carrier diagram represents the relation between RH and AH with respect to temperature [9].

In the above diagram, each line represents a 10 % increment of relative humidity. A cubic meter volume of air with 20 ℃ will be saturated with 17 g of water vapor. Additional water will compress as dew [9].

2.2. Temperature-humidity sensors

Temperature-humidity sensors are playing a major role in different areas including the medical industry and semiconductor industry. Moisture in the air deeply influences the processes of manufacturing, especially during wafer processing. Relative humidity must be monitored constantly to avoid air bubbles and water vapors. Some humidity sensors are also used for wearables to monitor the sweat, respiration, and skin moisture to prevent health diseases of the users [10].

Resistive temperature sensor is a common type of temperature sensor, which measures temperature by changing the resistance of a metal wire. Similarly, the capacitive humidity sensor is a common type of humidity sensor which measures humidity by measuring a change in the dielectric material. Both sensors are described in this study.

Besides these sensors, further different temperature-humidity sensors such as resistive humidity sensors and thermal conductivity sensors are also used in various fields [11]. But these are not working on the same principle as the EMFT sensors, therefore these are not described in this report.

2.2.1. Resistive temperature sensors

Resistive temperature sensors are used to measure atmospheric temperature in different environments. Typically, resistive temperature sensors are primarily a long, small diameter metal wire wrapped in a coil or an etched pattern on a substrate, similar to a strain gage as shown in Figure 2.2.

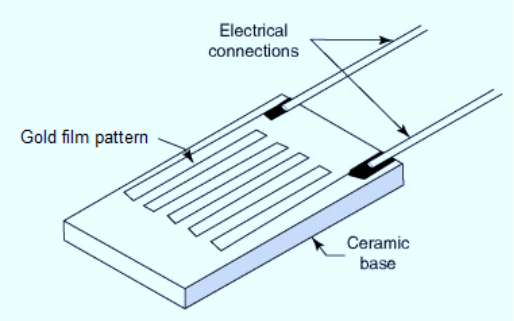

Fig. 2.2: Schematic view of a resistive temperature sensor consists of a gold film pattern placed on a ceramic base [12].

Resistive temperature sensors work on the principle that the electrical resistance of metals such as platinum, copper, or gold varies predictably with temperature in an essentially linear and repeatable manner. The specific resistance of most conductive materials varies with temperature. This is why particular resistance statistics are always given at a constant temperature typically at 25 °C. Temperature coefficient of resistance (TCR) is the resistance-change factor per degree Celsius of temperature change. The Greek lower-case letter alpha (α) represents this factor that can be calculated by the following formula [13].

$$TCR = \alpha = \frac{R - R_{ref}}{R_{ref} * (T - T_{ref})} \qquad Eq: 2.4$$

A positive coefficient for a material indicates that its resistance increases as temperature rises. Pure metals often have positive temperature coefficients of resistance. Certain metals can be alloyed to produce coefficients close to zero.
A negative coefficient for a material indicates that its resistance reduces as temperature

rises. Carbon, silicon, and germanium are examples of semiconductor materials with negative temperature coefficients of resistance.

The resistive temperature sensor plays a major role in different applications including electrical home appliances, the medical industry as well as power plant industry that contains hazardous environments. The resistive temperature sensors are significantly more stable and can provide accurate and exact readings for an extended period [14]. The resistive temperature sensor that is characterized in this thesis is made of gold wire because of its high sensitivity and good thermal conductivity. The temperature coefficient of resistance of gold is 0.0037 $°C^{-1}$. It can operate up to 400 ℃ temperature without any changes in its thermal and mechanical properties. The length of the gold wire used in this work was in the range of millimeters.

2.2.2. Capacitive humidity sensors

A capacitive humidity sensor determines relative humidity by varying the capacitance produced by changing the properties of a dielectric material which acts as an insulator. Ideally, the dielectric materials are hygroscopic, which can absorb and desorb water vapor from the atmosphere. The dielectric constant, which is also known as permittivity of insulating material, changes by continuous absorption of water vapor. This is due to the high dielectric constant of water which is around 80, as compared to the dielectric constant of insulating materials which is in the range of 1 to 4. Therefore, the dielectric constant of the insulating material increases by adsorbing water vapor, which induces a change in capacitance, and when the capacitance changes the impedance also changes which can be used to derive the humidity. When the RH changes typically from 5 % RH to 95 % RH, the resistance of the dielectric material also changes which corresponds to the change in permittivity [15].

Capacitive humidity sensors are usually fabricated as parallel plate capacitors or as inter-digital transducers IDTs. IDTs are comb-like structures made by two metal electrodes placed on a substrate where the insulating material is deposited on the top as a thin layer. The EMFT temperature-humidity sensors used in this thesis are also fabricated as comb-like IDT structures, as described in Section 3.1. If the sensors are fabricated in thin form, the change in impedance caused by humidity can be achieved on a large scale. Because the thinner the sensor with a certain thickness of insulating material, the easier for humidity to absorb and desorb by the material. Also, drying time will be shorter for the sensors after usage and can be calibrated easily after fabrication [16]. The insulator is typically a polymer which can withstand high temperatures without any mechanical changes mostly less than 400 °C. A capacitive

humidity sensor is ideal for use in harsh environments such as high temperatures or temperatures below 0 °C. Furthermore, it does not require any maintenance for an extended period of time, is easy to use, and is not affected by atmospheric pressure. It provides an accurate output with high sensitivity and with a wide range of relative humidity, even at low humidity levels these sensors respond actively. But it does not have long-term stability and is also sensitive to dewing and some aggressive substances [17]. Figure 2.3 shows a schematic representation of a capacitive humidity sensor which shows the placement of a comb-like structure of two IDT metal electrodes on a substrate with a humidity sensing layer.

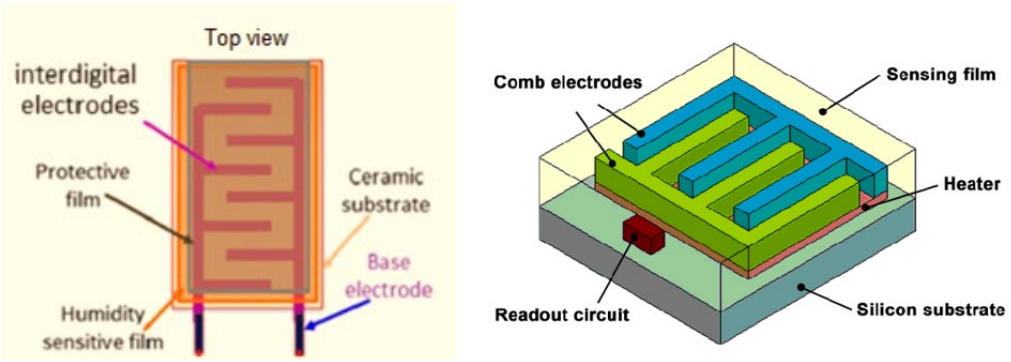

Fig. 2.3: Schematic representation of capacitive humidity sensor [18, 19].

2.3. Polyimide sensing layer

Polyimide is a polymer that can also be used as a dielectric sensing layer for humidity sensors. It carries an imide group. Its chemical structure can be either linear or cyclic [20]. Mostly, the cyclic structure of PI is commercially used due to its stable and excellent electrical, thermal and mechanical properties in a corrosive environment which makes it an ideal material for high-performance applications. PI has good mechanical properties because of the stiffness of scented segments in the repeating units and the strong intermolecular forces between polymer chains [21]. A typical polyimide chemical structure is shown in Figure 2.4.

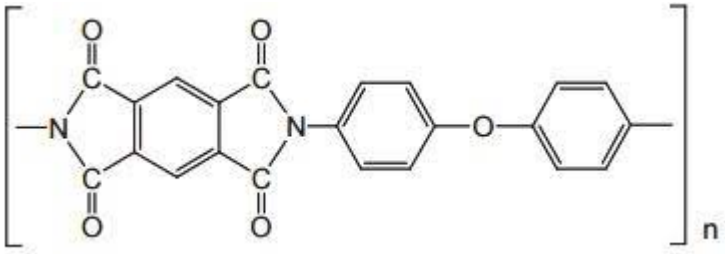

Fig. 2.4: General chemical structure of polyimide (PI) polymer attached with imide-groups [22].

The charge transfer complexation is also an important part of polyimide. The material needs to be compatible with both donor and acceptor segments. In the PI the electron-rich nitrogen group serves as a donor, while the carbonyl group serves as an acceptor, which lends some electrons from the donor. In this way, two segments are tightly bound to each other and even multiple chains can be developed [23]. The PI sensing layer characterized in this study is prepared from Fujifilm's Durimide 7500 Photosensitive Polyimide Precursor. This precursor obtains a liquid amido carboxylic that reacts with the methacrylic acid to glycol. This glycol is applied by spin coating and then hardened by exposure and can be thermally transferred to PI. Because of its fine porous structure, water vapor can penetrate the PI layer and effect to change the electrical properties which makes it an ideal insulator for capacitive humidity sensors. PI are hydrophilic in nature that absorb more moisture [24].

2.4. Polarization mechanisms of PI

Charges don't move freely from one electrode to another inside the Polyimide due to strong intermolecular forces. When an electric field is applied to a capacitor that contains polyimide as an insulator, a dipole moment is created inside the PI in which positive charges align with the electric field and negative charges align in opposite direction. This pure effect can be explained as polarization. A capacitor can store more charges if an insulating material can easily be polarized [25]. There are four different mechanisms of polarization [26]:

- Electronic or atomic polarization.
- Orientation or dipolar polarization.
- Ionic polarization.
- Interfacial polarization.

2.4.1. Electronic polarization

This mechanism can usually be found in all ions or atoms. When an electrical field is applied it forces the nucleus and its electron cloud to distort from each other. Thus, a very weak dipole is produced as a result of a very small effect of polarization in which a positively charged nucleus is aligned with the electrical field while the negatively charged electrons are aligned against it [27]. This electronic polarization is very rapid in the process. Therefore, it activates at frequencies around 10^{17} Hz [28]. The whole

representation of this electronic polarization is shown in Figure 2.5.

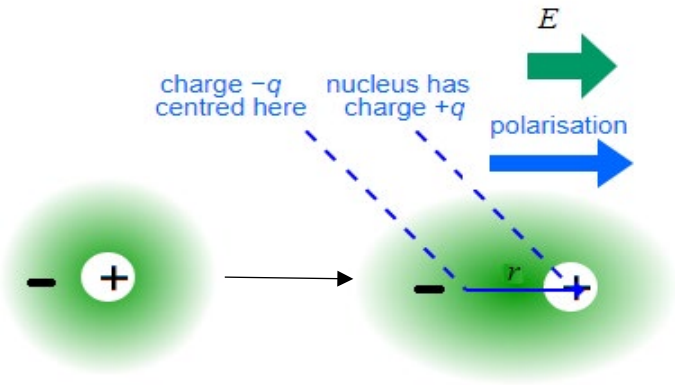

Fig. 2.5: Image of electronic polarization of atom [29].

2.4.2. Orientation or dipolar polarization

This polarization is very common in polymers in which molecules possess permanent dipoles containing a charge separation even without an electric field. These dipoles are arranged randomly in non-polar materials. Thus, the dipole moments from different molecules cancel out and the net polarization is zero. When an electric field is applied, the dipoles rotate to align in the same direction as the electric field. Therefore, they also align with each other. A net polarization creates as dipole moments can no longer cancel out [30]. This dipolar polarization occurs at frequencies below 10^{10} Hz [28]. The whole representation of this orientational polarization is shown in Figure 2.6.

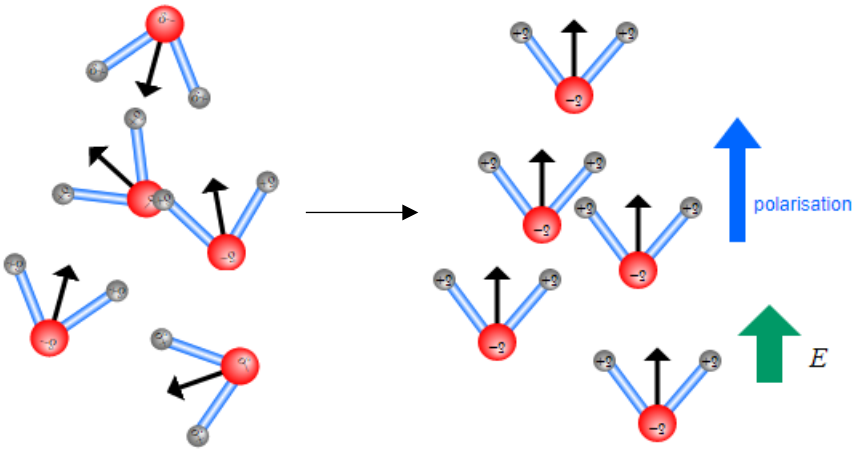

Fig. 2.6: Representation of orientational or dipolar polarization [29].

2.4.3. Ionic polarization

Ionic structures are composed of cations and anions with ionic bonds in which ions are symmetrically arranged inside a crystal lattice with zero net polarization. But when an electric field is applied, ions start to be displaced in the opposite direction which produces a net dipole moment [31]. Ionic polarization occurs at frequencies of around 10^{13} Hz slightly slower than electronic polarization [28].

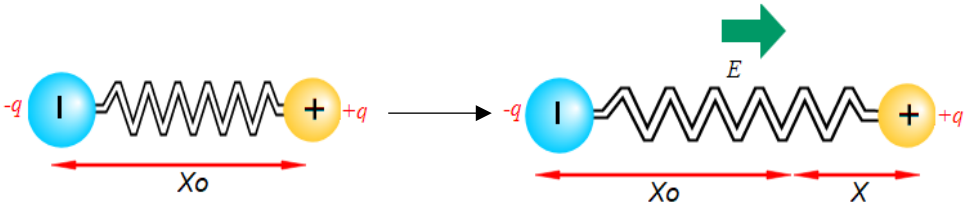

Fig. 2.7: Image of ionic polarization [29].

2.4.4. Interfacial polarization

This polarization has a different mechanism in comparison to the above three polarizations. Instead of only bound positive and negative charges it also affects the free charges inside the material. This polarization is also known as space charge polarization, as it accumulates charges and interfaces between two different materials or at grain boundaries inside a material. Because charges follow an electric field rather than maintaining their charge neutrality [32]. Can be visualized in Figure 2.8.

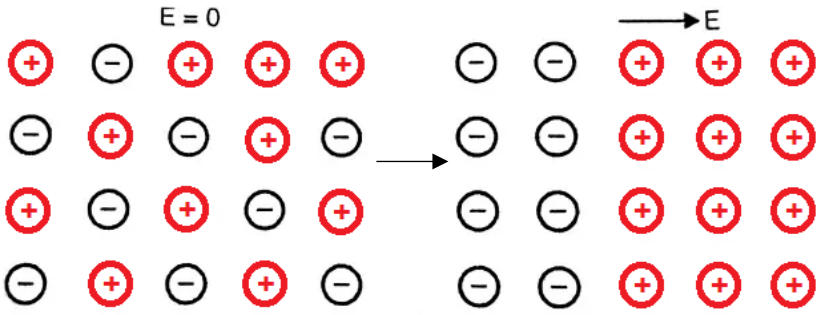

Fig. 2.8: Visualization of interfacial polarization [29].

Usually, this kind of polarization is observed in polycrystalline or amorphous solids. Because of the slow mechanism, it occurs at frequencies below 10^4 Hz [28].

3. Material and Methods

In this section, the designed structure and layout of two EMFT temperature-humidity sensors are described, which are distinguished as sensor A and sensor C due to the change in pitch of the IDTs and the width of the temperature sensor. After that, the procedure for measuring the electrical characteristics of the EMFT humidity sensor in both alternative current (AC) and direct current (DC) on a wafer probe analyzer is described. Then the working mechanism of the HAST system is explained. In the end, the electrical specifications and operating mechanisms of two selected reference sensors are discussed.

3.1. EMFT sensor Layout

The layout of humidity sensors A and C were developed and produced in a clean room by the EMFT itself. The wafer used was 500 µm thick and 6 inches in size. The material of choice was Borosilicate as the substrate of the wafer. Because it has a low dielectric constant which is $\epsilon = 4.6$ with a thermal expansion coefficient of $\alpha = 3.3 \times 10^{6}\ K^{-1}$ which is 60 % less than compared to quartz glass [33]. A schematic view of both sensors A and C can be seen in Figure 3.1.

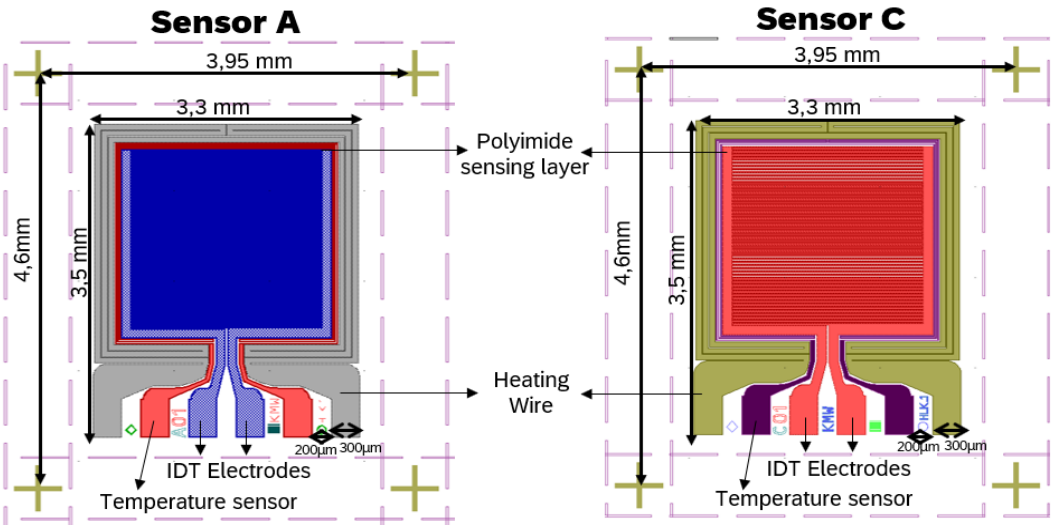

IDT´s pitch	14 µm • Gap between electrodes=6µm; • Electrodes width=8µm
Temperature sensor width	13 µm

IDT´s pitch	18 µm • Gap between electrodes=8µm; • Electrodes width=10µm
Temperature sensor width	12 µm

Figure 3.1: Schematic view of EMFT temperature-Humidity sensors A and C layouts.

Firstly, a 35 nm thin adhesive layer of Titanium Tungsten (TiW) is spattered onto the wafer followed by a sputtered 150 nm thin gold layer. To structure the gold layer a photo resistive mask was applied on top of it. Afterward, the wafer was wet etched with aqua regia and tempered at 400 °C. Finally, the wafer was coated with a PI sensing layer by using a spin coater. The thickness of the PI was in the range of µm. In the end, the wafer was diced into 3.95 mm x 4.6 mm pieces in which the size of both sensors was 3.3 mm x 3.5 mm.
Each sensor consists of two electrodes ordered in a comb-like IDT structure working as a capacitor, a gold wire for resistive temperature measurements as well as a heating wire to heat the sensor. Both sensors differed concerning the IDT's pitch which is 14 µm and 18 µm respectively, in which the gap between two electrodes is 6 µm and 8 µm and the width of electrodes is 8 µm and 10 µm respectively. Similarly, the resistive temperature wire used for simultaneously measuring the atmospheric temperature also had different widths which are 13 µm and 12 µm respectively. Otherwise, the geometry and the dimensions of both sensors were similar.

3.2. Wafer probe analyzer

For electrical measurements, the EMFT temperature-humidity sensors were placed on a wafer probe analyzer where capacitance, conductance, resistance, and the current were measured concerning the range of different frequency and bias voltage at different temperatures. Figure 3.2 shows the whole setup of the wafer probe analyzer and the connections of wafer probes with the EMFT humidity sensors can be seen in Figure 3.3.

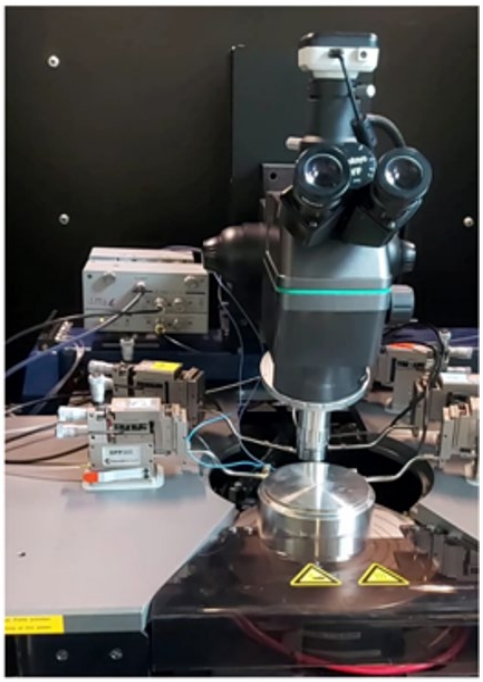

Figure 3.2: Setup of wafer probe analyzer.

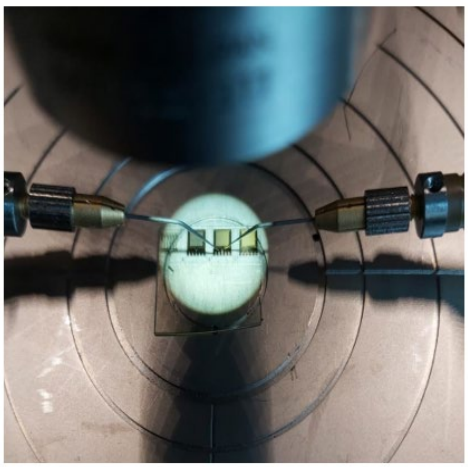

Figure 3.3: EMFT sensors connected with wafer probes.

The wafer prober is used to characterize the wafer to make contact in the designated position on the device. A wafer prober is a tool used for testing circuits and devices on wafers, dies, and open microchips. It is also known as a semiconductor probe station or probe station.

Users can place electrical, optical, or RF probes on a wafer using wafer prober stations to evaluate the device under test (DUT). These tests might be basic, like a continuity or isolation check, or complex, like a full functioning test of a microcircuit. The wafer can be seen in individual dies before or after tests are conducted.

Manufacturers can test a device several times throughout the manufacturing process by testing at wafer level with a wafer prober. This gives information about the process steps which result in flaws in the final product. Additionally, it gives manufacturers the chance to test the dies before packing them, which is crucial in applications where the price of packaging is high compared to the price of the device [34].

In this study, the dies of EMFT sensors were placed on the wafer chuck. The wafer probes were connected to the pads, and signals were transmitted to the system. The measurements of capacitance, conductance, resistance as well as I-V sweep curves were displayed on the computer. The wafer chuck was also connected to a temperature controller which regulated the temperature as needed. Using a camera or a microscope, it was easy to connect the probes to the electrodes. Figure 3.4 shows the complete operational cycle of the wafer probe analyzer.

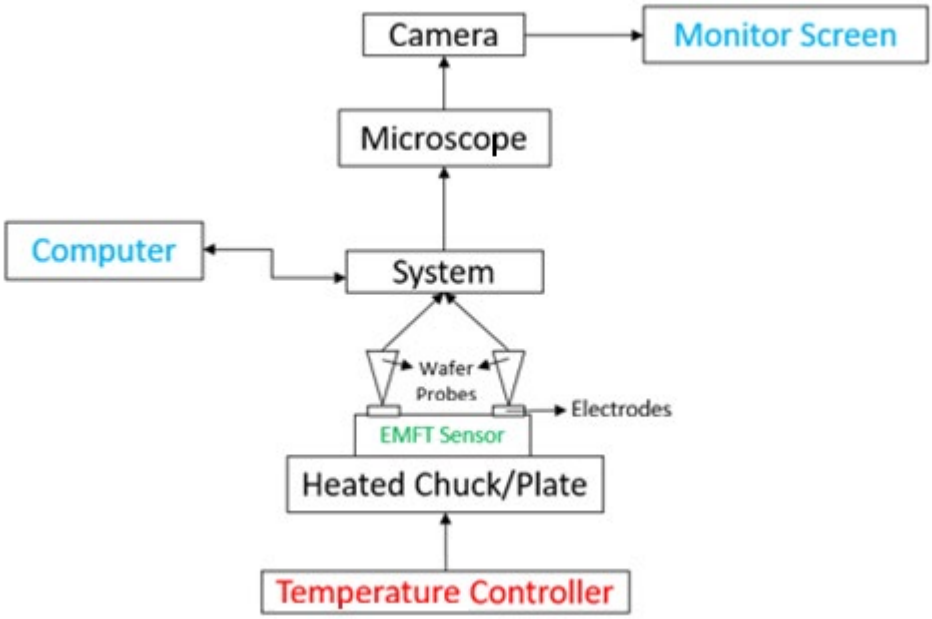

Figure 3.4: Block diagram of the working process of a Wafer Probe analyzer.

3.3. Highly Accelerated Stress Test (HAST) system

In this thesis, the Highly Accelerated Stress Test (HAST) system "EHS-221MD by Espec",

which complies with IEC60068-2-66 and other international requirements for bias testing was used to conduct the humidity stress tests. The EHS-221MD HAST system, as shown in Figure 3.5, has two independent chambers which may operate independently on various settings as well as an operator control panel for setting up parameters to perform the test. Each chamber has an inner cylinder with an arched ceiling to prevent condensation from dripping on the specimen when the chamber begins to cool. Signal terminals within the chamber connected the sensor to the terminal outside on the right. From there the DUT was connected with the SMU (Source Measuring Unit) by "HK Testsyteme", which was further connected to the computer with the test software through a serial to USB adapter.

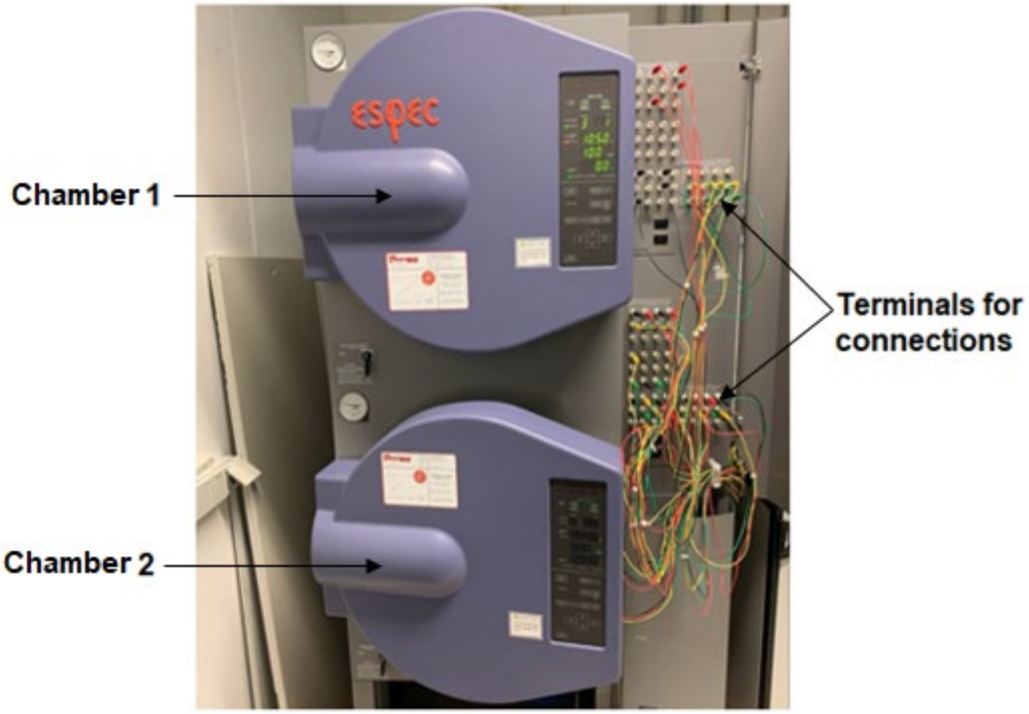

Figure 3.5: The Highly Accelerated Stress Test (HAST) System contains two chambers with outside terminals to connect the specimen with the external test equipment.

The rack is loaded onto a shelf inside the chamber. Wet-and-dry bulb temperature control, wetting saturation control, and unsaturated control are three test conditions of the HAST chamber. Wet-and-dry bulb temperature control uses a wet-and-dry bulb temperature sensor to directly detect and regulate the test chamber temperature and humidity. When testing with wetting saturation control, the HAST chamber heater is turned off and only the humidifying heater is regulated. While in unsaturated control, the HAST chamber heater produces a slight inclination towards unsaturation [35]. The chamber contains a temperature sensor which is placed at the back of the chamber to measure the temperature. Relative humidity is monitored by a dry and wet bulb temperature control mode. Therefore, a linen sock is wrapped around a second

temperature sensor which is located in front of the vessel. The sock absorbs moisture during the measurements. Due to the adiabatic evaporation, the sensor measures at a slightly cooler temperature than the unwrapped sensor placed at the back of the chamber. The temperature difference between these two sensors is correlated to the relative humidity inside the chamber. As well as the shelf including the mounting for the PCB is placed inside the inner cylinder, one inner terminal is on the left and connected to the mounting of the PCB. In Figure 3.6. the inner view of the chamber as well as the placement of the sensors can be seen.

Figure 3.6: Inner view of the chamber of the HAST system EHS-2221MD.

The values for temperature, relative humidity, operating period of the test as well as the different modes can be programmed through the operator control panel. One can choose between the program mode or the constant mode, while the unsaturated and wet saturated control can be chosen for both program and constant modes. The dry and wet bulb temperature control mode can only be chosen when the program mode is used [36]. As the name suggests, one may program several stages to perform the test while using program mode. Each step may be set with a different temperature and relative humidity value as well as a varied time. Used in constant mode, temperature and RH are fixed throughout the whole test run.

Before the chamber reaches the selected temperature and RH specifications, the operating period of the test is not initiated. Since ramp-up time is only taken into consideration at the beginning of program mode use, it is important to take this ramp-up procedure into account. Therefore, if the temperature is increased from one step to the next while using the program mode, the time for the ramp-up process is not considered by the system itself. The time required for the ramp-up step must be added to the intended duration for this particular phase.

After adjusting the desired test settings, the door has to be locked. This is to ensure

the chamber is hermetically sealed and the pressure inside is maintained. But before the test run can be started, one has to start the test software for simultaneous data logging. The SMU was provided by "HK Testsysteme" which provides a constant DC voltage of up to 30 volts. The electrical specifications of the SMU can be seen in table 3.1.

Voltage range	Current range	Accuracy
0 - 30 V	0-1000nA	+/- 10nA
	0-1000µA	+/- 1µA
	0-10mA	+/- 10µA

Table 3.1: Electrical specifications of SMU (Source Measuring Unit).

Because the current measurement can be in the range of a minimum of 10 nA the voltage has to be extremely stable to minimize the measuring inaccuracy. The SMU can provide a constant voltage to thirteen isolated power supplies simultaneously with a permitted inaccuracy of 0.1 V, which can be seen in Figure 3.7.

Figure 3.7: SMU (Source Measuring Unit) consists of 13 independent voltage sources provide DC voltage up to 30 V with 10 nA max resolution.

The test software can therefore operate each voltage source independently. A group of power units must be generated within the software before the measurement can begin. This group of power units can be used for the next measurements. Since the system may either utilize a single power unit or the assembled group of several power units, all necessary power units must be combined into a single group. The actual measurement parameters can then be chosen from this group. The applied voltage and the current range for the measurement both have to be set in the measurement parameters. The connected power unit will shut down to protect the SMU if an

excessive current is detected during the test. The software only allows a maximum current of 10 mA and a maximum DC voltage of 30 V.

In this study for the HAST measurements, the Temp-Humidity sensors A and C were glued and wire bonded to C-DIPs (Ceramic Dual Inline Packages). C-DIPs are commonly used for integrated circuits where high temperature or reliability are required, or when the device has an optical window to the package's interior. Most C- DIPs are soldered to a PCB after the pins are inserted through holes on the board. Ceramic packages are less physically constrained than other materials, which improves the product's performance. Ceramics packages increase a product's lifespan as they are corrosion- and wear-resistant. Mostly ceramic packages are used for test purposes and are rarely used for final products as they are expensive. The C-DIPs were connected with a Teflon-gold PCB through a mounting hole. Four sensors, two sensors A and two sensors C, each inside a C-DIP were connected to Teflon-gold PCB, as shown in Figure 3.8.

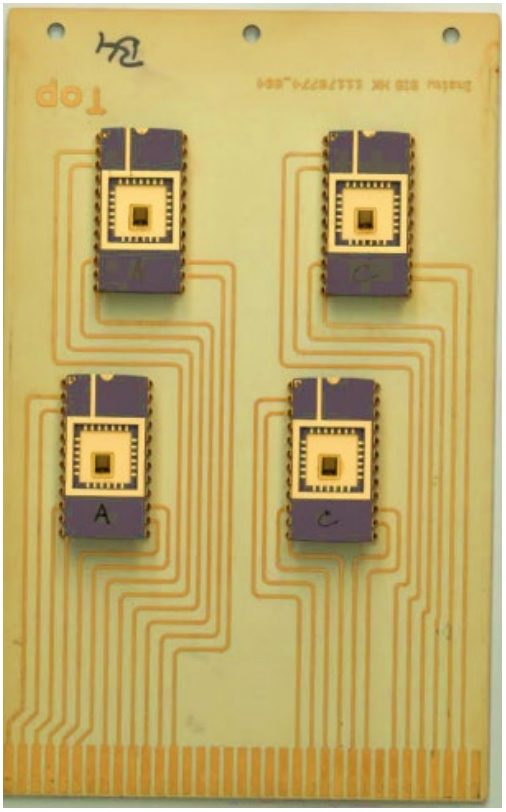

Figure 3.8: Sensors A and C were glued, wire-bonded to C-DIPs, and connected with Teflon-gold PCB through a mounting hole.

The HAST chamber was operated in constant mode under three different conditions, which are as follows:

Ramp-up: The chamber began the ramp-up process where the temperature rose to 130 °C and the relative humidity reached 85 % RH. The actual measurement was started

after finishing the ramp-up process.

Step 1: The temperature was set to 130 °C and the RH to 85 % for 100 hours.

Cool down: The measurement was done and the pressure inside the chamber decreased. Resulting in a decreasing temperature and RH.

3.4. Reference Temp-Humidity sensors

A comparison of two calibrated temperature-humidity reference sensors with the HAST built-in sensors was performed to monitor the actual temperature and relative humidity inside the HAST (Highly Accelerated Stress Test) chamber. As already explained in Section 3.3 that the difference between the temperature sensor and the linen sock-wrapped temperature sensor was referred to as relative humidity.
Due to this inaccurate method for measuring the relative humidity of the HAST chamber, it was decided to integrate the relative humidity with two calibrated humidity sensors placed inside the chamber through Teflon-gold PCB, to ensure that the temperature and relative humidity were correct as given by the HAST built-in sensors on dry and wet bulb mode. The calibrated reference sensors were used because of the prerequisite of accurate and reliable monitoring of the HAST chamber.
Two calibrated reference sensors were selected which were in principle similar to the EMFT temperature-humidity sensors. Both reference sensors contained a capacitive humidity sensing element and a resistive temperature sensor with a polymer sensing layer. One was 'HTU31D sensor by TE Connectivity and the other was 'BME280 by Robert Bosch GmbH', as shown in Figure 3.9.

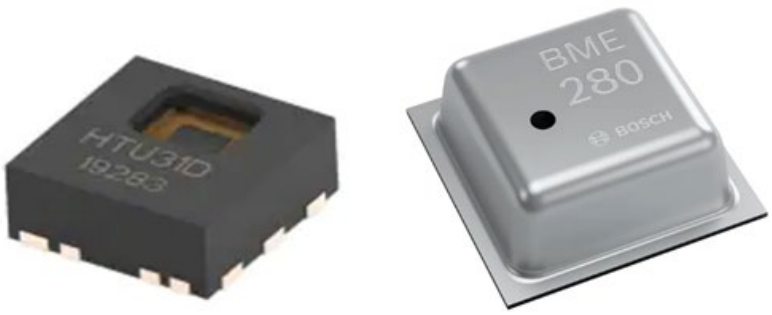

Figure 3.9: Selected reference sensors HTU31D and BME280 with the same principle as EMFT Temp-Humidity Sensors [36, 37].

The HTU31D humidity sensor developed by TE connectivity could operate in a range of 0 % RH to 100 % RH relative humidity with a temperature range of -40 °C to +125 °C. The sensor can interface with a microcontroller via an I2C address, with a wide

supply voltage range from -3.0 V to 5.5 V. The sensor was designed as a compact 6-pin DFN (dual flat no-lead) surface mount package containing a PI sensing layer, with a dimension of 2.5 mm x 2.5 mm x 0.9 mm [37].

While the BME280 humidity sensor was manufactured as a metal lid LGA (land grid array) by Robert Bosch GmbH company with the same dimensions of 2.5 mm x 2.5 mm x 0.93 mm. It has the same relative humidity range as the HTU31D sensor which is 0 to 100 % RH, while the temperature range is slightly lower from -40 °C to 85 °C. The sensor can also interface with a microcontroller via an I2C address, with a voltage range of 1.2 V to 3.6 V [38]. The schematic layouts of both reference sensors can be seen in Figure 3.10.

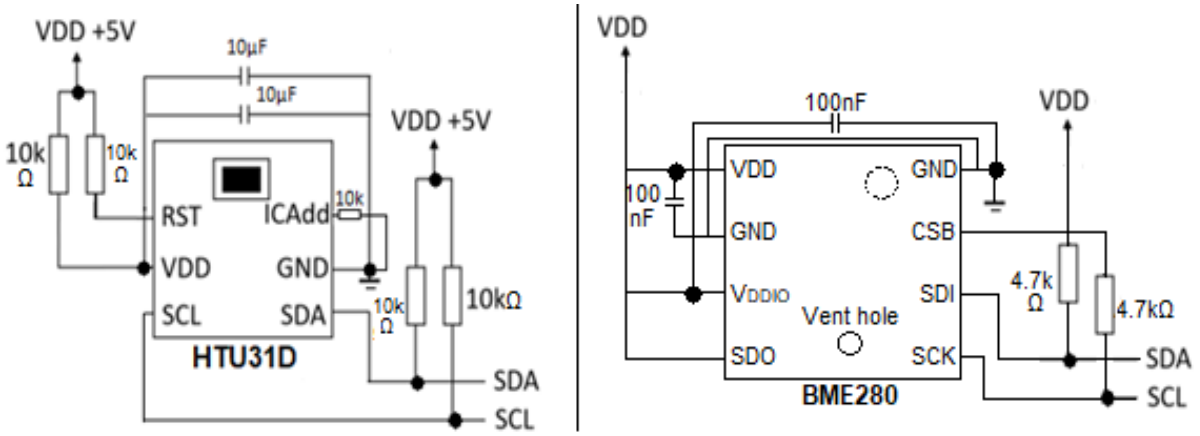

Figure 3.10: Schematic design of both reference sensors HTU31D and BME280, to place on Teflon-gold PCB inside the HAST chamber [36, 37].

To operate these reference sensors with a microcontroller, breakout boards were used with built-in reference sensors. Breakout boards are used to readily connect small sensors, chips, and components to any microcontroller, including the Raspberry Pi, Metro, Feather, Arduino, and more. To facilitate prototyping and experimentation with the integrated circuit, a breakout board separates the pins of these surface mount ICs onto a PCB with output pins that are correctly spaced for a solder-less breadboard. The basic idea of a breakout board is to simplify the use of a single electrical component [39].

The first breakout board for the HTU31D sensor was chosen from the open-source hardware business Adafruit Industries, while the second breakout board was produced by the Pimoroni hobbyist electronics company for the BME280 sensor. Because of these breakout boards, the reference sensors were limited to operating at 85 % relative humidity and 85 °C temperature. Because above 85 °C temperature could cause the burning of components or boards. In Figure 3.11, Both reference sensors with breakout boards can be seen.

Figure 3.11: HTU31 sensor breakout board by Adafruit and BME280 sensor breakout board by Pimoroni respectively [40, 41].

Since the breakout boards of both reference sensors could be interfaced via an I^2C address, an Arduino Uno microcontroller was used to operate these reference sensors one after the other. As the Arduino libraries for each sensor module were readily available. The code was written on Arduino software for each sensor and uploaded to the Arduino microcontroller through a USB port connection between the laptop and the board.

After uploading the code, the hardware connection was created between the pins of the reference sensors board (SCL & SDA) and the Arduino Uno board (A5 & A4) to transmit and receive signals for serial communication. The data was stored in a text file with date and time stamps. Figure 3.12 represents the connections between the Arduino Uno microcontroller and the reference sensors breakout boards.

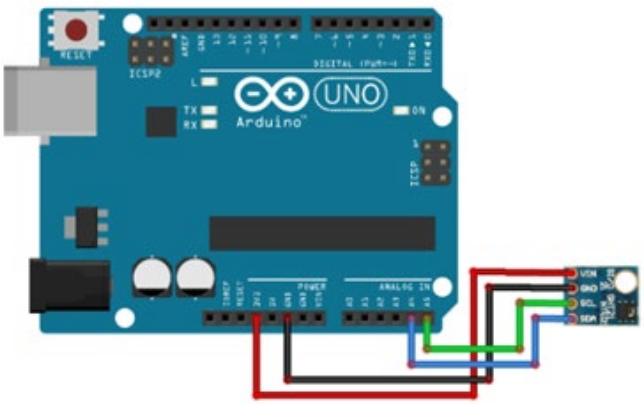

Figure 3.12: I^2C interfacing between Arduino microcontroller and reference humidity sensors [42].

After initial testing, reference sensors with breakout boards were installed on a rack inside the HAST chamber with Teflon-gold PCB as shown in Figure 3.13.

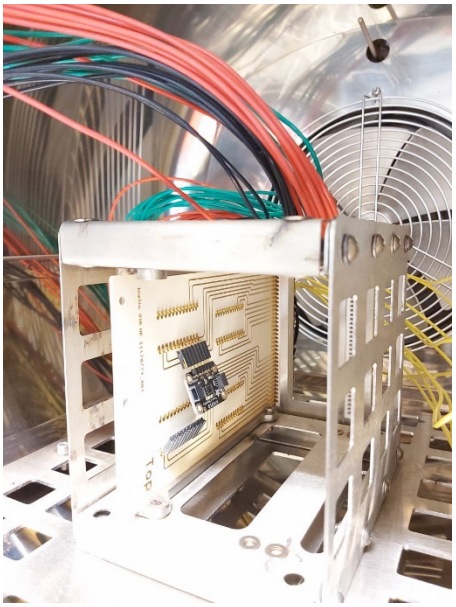

Figure 3.13: Installed reference sensor with PCB Teflon inside the HAST chamber.

Signal terminals inside the chamber connected the sensors to the outside terminals of the HAST and from there they were connected one after the other to the Arduino Uno microcontroller. The HAST chamber was operated in a constant mode for 8 hours where the temperature was set up to 85 °C temperature with 85 % relative humidity. Initially, the chamber began a ramp-up process for 2 hours, where the temperature rose to 85 °C and the RH inside the chamber reached 85 %. After the ramp-up process was over, the actual measurements were started for 6 hours.

4. Results

This section begins by presenting the results of electrical measurements of EMFT humidity sensors A and C which were performed on a wafer probe analyzer. Then the comparison of the HAST chamber sensors with the reference sensors is displayed. In the end, the results of EMFT sensors A and C measurements inside the HAST chamber are given.

4.1 Wafer probe measurements

The electrical characteristics of EMFT humidity sensors A and C as defined in section 3.1, were measured with a wafer probe analyzer in both AC and DC modes and the effects of different temperatures on the resistance of both temperature sensors A and C were also observed. In the beginning, the capacitance was measured of both humidity sensors A and C at three different temperatures 25 °C, 85 °C, and 130 °C respectively in a frequency range of 1 kHz to 1 MHz with an amplitude of 250 mV AC with a fixed bias voltage of 30 V DC as shown in Figure 4.1.

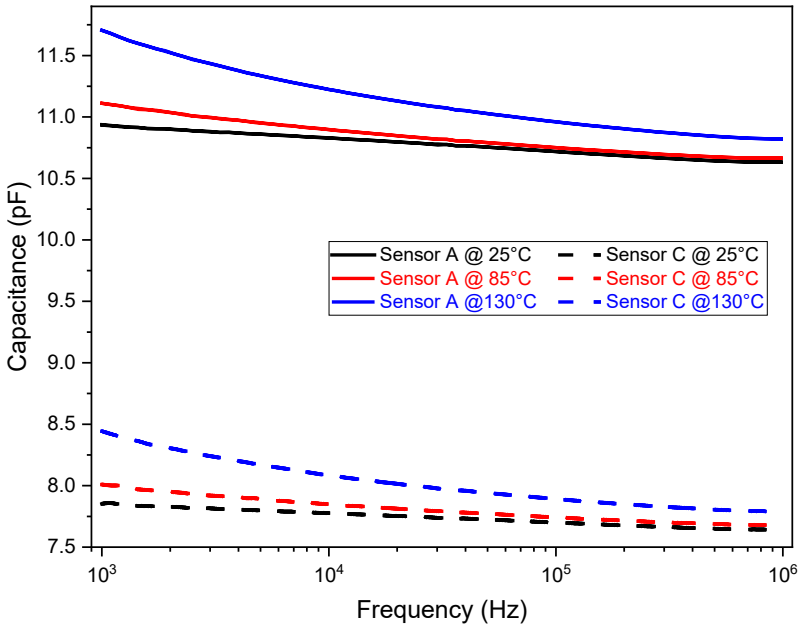

Figure 4.1: Generic C-f measurements of both humidity sensors at 30 V DC with 250 mV AC amplitude.

Sensor A provided higher capacitance measurements as compared to Sensor C. This is due to the difference in the pitch of the IDTs of both sensors, where the width of electrodes and the gap between them were not similar, as explained in section 3.1. Both humidity sensors A and C had similar responses. The capacitance exponentially decreased as the frequency was increased from 1 kHz to 1 MHz. This was due to the change in impedance across the IDT electrodes of sensors. The impedance occurred because the electrons on IDT electrodes appeared in the form of electric charge to move more rapidly from one electrode to another with respect to different frequencies [43]. On the other side, As the temperature increased the capacitance of the sensors was also increased. This was due to the change in dielectric properties of the PI layer that covered the IDT electrodes of humidity sensors and was working as an insulator. The values of capacitance were in the range of pF which represented the efficiency of the polyimide layer to absorb the high energy.

After monitoring the temperature and frequency responses of both sensors, the capacitance and conductance of both humidity sensors A and C were investigated at again three different temperatures of 25 °C, 85 °C, and 130 °C but with a fixed frequency of 1 kHz and in the bias voltage range from -30 V to +30 V DC in 0.3 V steps. The result can be seen in Figure 4.2.

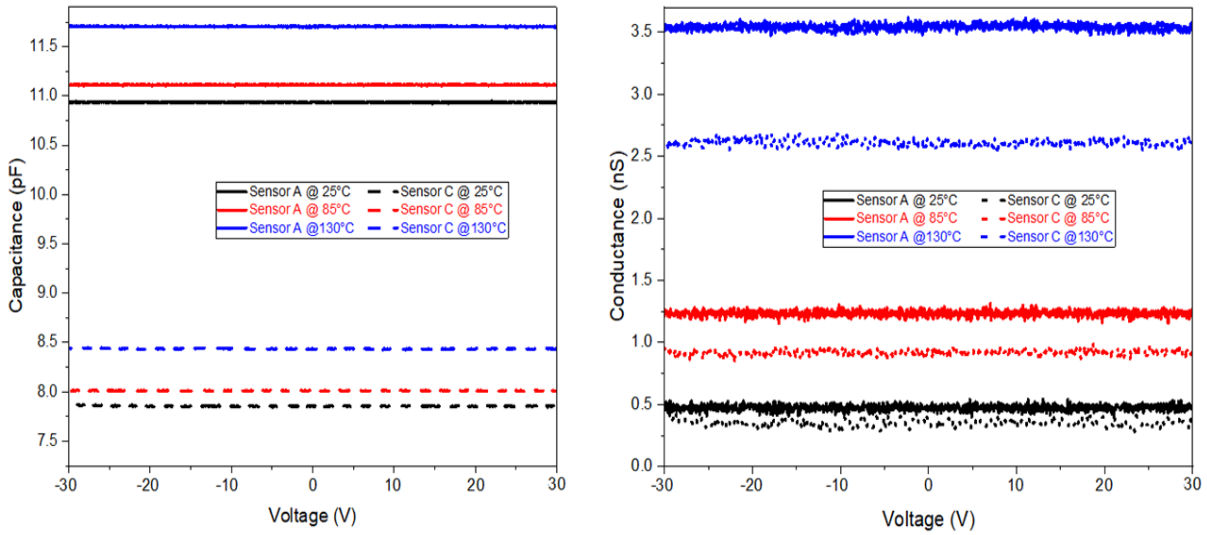

Figure 4.2: Capacitance (C-V) and conductance (G-V) measurements at three different temperatures of both humidity sensors A and C at a fixed frequency of 1 kHz and in the bias voltage range from -30 V to +30 V DC in 0.3 V steps.

The capacitance of both sensors A and C remained constant at different applied voltages, because by adding a certain number of charges to the IDT electrodes its voltage also increased, therefore the capacitance remained constant [44]. The conductance values of both sensors were also the same at different applied voltages. Because the polyimide layer's conductivity remained constant due to its isotropic

composition [45]. However, the increase in temperature was increasing the capacitance of the humidity sensors because of the change in the dielectric constant of the PI layer. Similarly, the conductance also increased as the temperature increased the kinetic energy of the ions and the ions carried their charge faster [46]. The conductance was in the range of nS with less noise. Most noises are produced in the current flow and conduction process by impurities in the material that can be reduced by providing a constant frequency [47]. Therefore, a 1 kHz constant frequency was applied during the measurements.

After measuring capacitance and conductance, current was measured in both humidity sensors with a limitation of 10mA current and with a bias voltage range from 0 V to 30 V in 10 mV steps at three different temperatures of 25 °C, 85 °C, and 130 °C. The result is displayed in Figure 4.3.

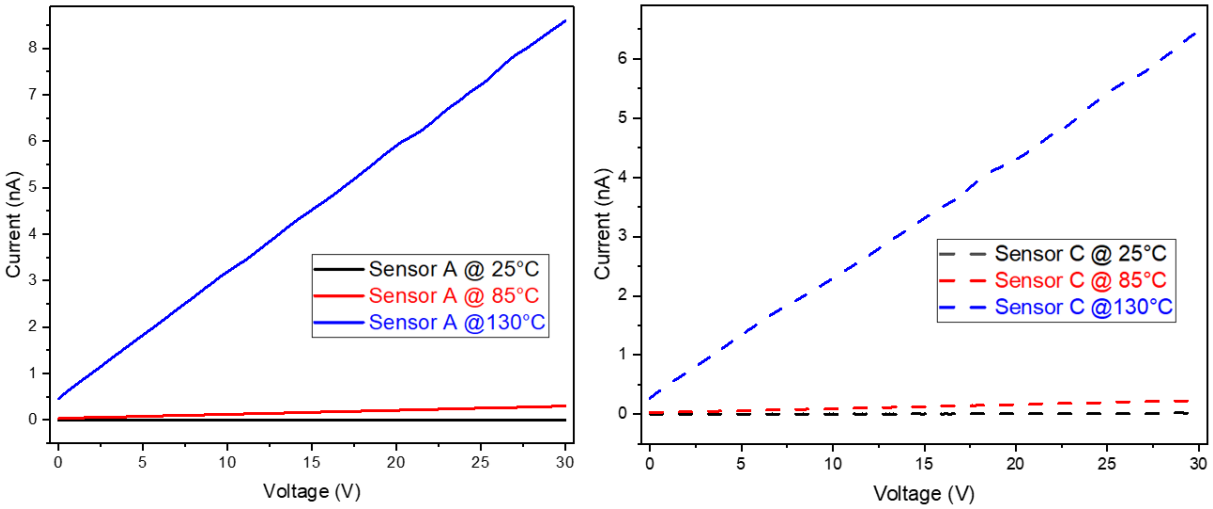

Figure 4.3: Current and voltage (I-V) characteristics at three different temperatures of both humidity sensors A and C with a limitation of 10 mA and in a bias voltage range from 0 V to +30 V DC in 0.1 V steps.

The current-voltage (I-V) characteristic curves presented the relationship between the current flow through the IDT electrodes underneath the PI layer and the voltage applied to the terminals of both humidity sensors. The ratio of applied voltage and the current flow were showing the resistance between the electrodes [48]. The current flow was very low at 25 °C because the resistance was very high across the IDT electrodes that validated Ohm's law. But as the temperature increased the resistance between the electrodes decreased due to the PI layer that acted as an insulator [49]. Hence, the current flow was rapid at 130 °C due to low resistance and the rapid movement of free electrons from one electrode to another as shown in Figure 4.3. The current values were in the range of nA. From the linear regression slope of each I-V characteristic curve, the conductance values of humidity sensors A and C were extracted at three different temperatures as shown in Table 4.1.

Temperature (°C)	Humidity Sensor A	Humidity Sensor C
	Conductance (pS)	Conductance (pS)
25	0.067	0.339
85	8.78	6.80
130	270.7	203.4

Table 4.1: Conductance values of both EMFT humidity sensors A and C were extracted from the linear regression slope of each I-V characteristic curve.

When the temperature increased, the conductance of both humidity sensors was also increased due to the ionization of charges between IDT electrodes. The conductance is inversely proportional to resistance. Therefore, an increased conductance means decreasing the resistance of humidity sensors.

After measuring all electrical properties of humidity sensors A and C. The current-voltage (I-V) measurements of temperature sensors A and C were performed for the resistive response. The limitation of current and the bias voltage range was the same as applied for humidity sensors, which is 10mA current and from 0 to 30 V DC in 10 mV steps. The current-voltage characteristic results of temperature sensors A and C are shown in Figure 4.4.

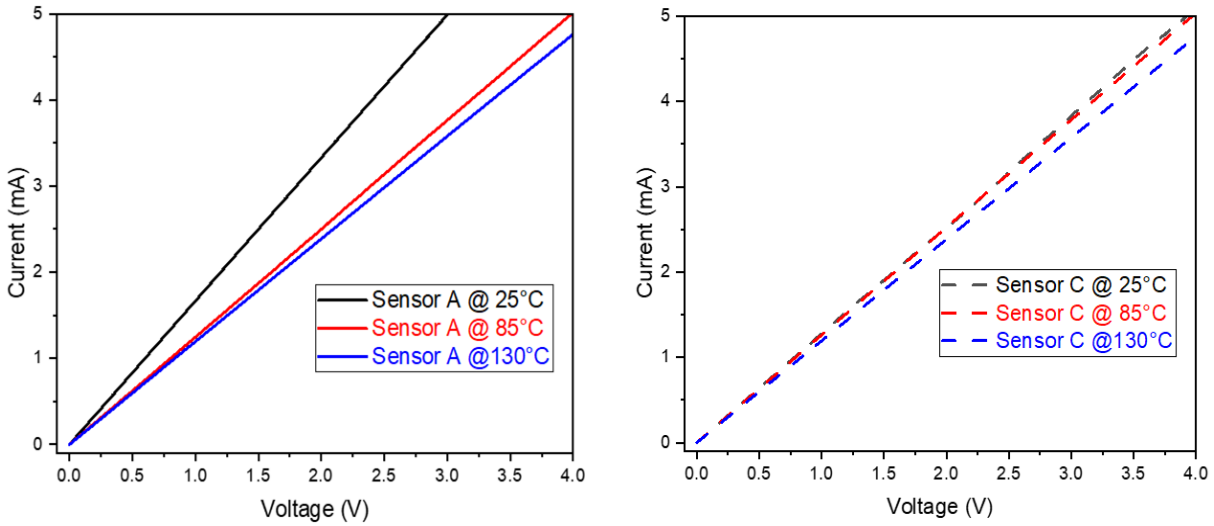

Figure 4.4: Current and voltage (I-V) characteristics at three different temperatures of both temperature sensors A and C with a limitation of 10 mA and in a bias voltage range from 0 V to +30 V DC in 10 mV steps.

The temperature sensors were made of gold metal wire, as already explained in Section 3.1. Therefore, as shown in Figure 4.4, when the temperature increased the resistance was also increased because the atoms of gold vibrated more due to heat which was

affecting the flow of electrons [50]. From the linear regression slope of each I-V characteristic curve, the conductance values of temperature sensors A and C were extracted at three different temperatures as shown in Table 4.2.

Temperature (°C)	Temperature Sensor A	Temperature Sensor C
	Conductance (mS)	Conductance (mS)
25	1.66	1.53
85	1.51	1.51
130	1.43	1.43

Table 4.2: Conductance values of both temperature sensors A and C were extracted from the linear regression slope of each I-V characteristic curve.

Conductance is inversely proportional to resistance. Therefore, When the temperature increased, the conductance of both temperature sensors A and C decreased due to the thermal motion of electrons [51], as shown in Table 4.2.

To further characterize the resistive response of both temperature sensors, bidirectional resistance was measured with a 5 mA current limit at six different temperatures: 25 °C, 50 °C, 70 °C, 90 °C, 110 °C, and 130 °C. The result is shown in Figure 4.5.

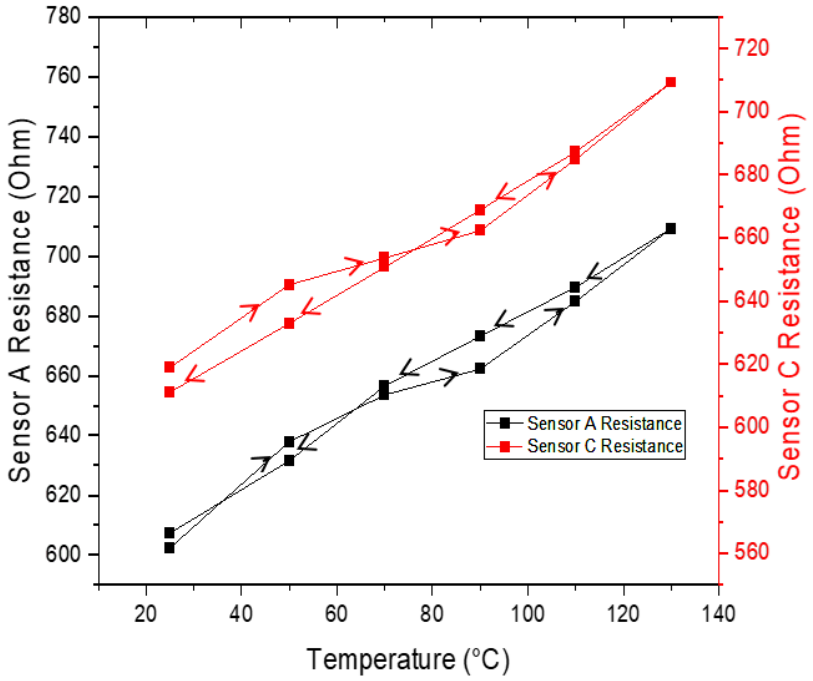

Figure 4.5: Resistive behavior of both temperature sensors A and C at heating and cooling temperature.

The resistive response of temperature sensors A and C was excellent concerning the temperature. As the temperature increased the resistance of both temperature sensors was also increased. Similarly, when the temperature decreased the resistance of both temperature sensors was also decreased, as displayed in Figure 4.5.

4.2 Reference sensors measurements

In the next part of the measurements, the temperature and humidity inside the HAST chamber were simultaneously monitored. The temperature and humidity measurements of each reference humidity sensor BME280 and HTU31D were compared with the measurements of HAST built-in sensors. The HAST chamber was operated in a constant mode for 8 hours at a temperature of 85 °C with a humidity set value of 85 % RH. The comparative measured results of both reference sensors BME280 and HTU31D are shown in Figures 4.6 and 4.7, respectively.

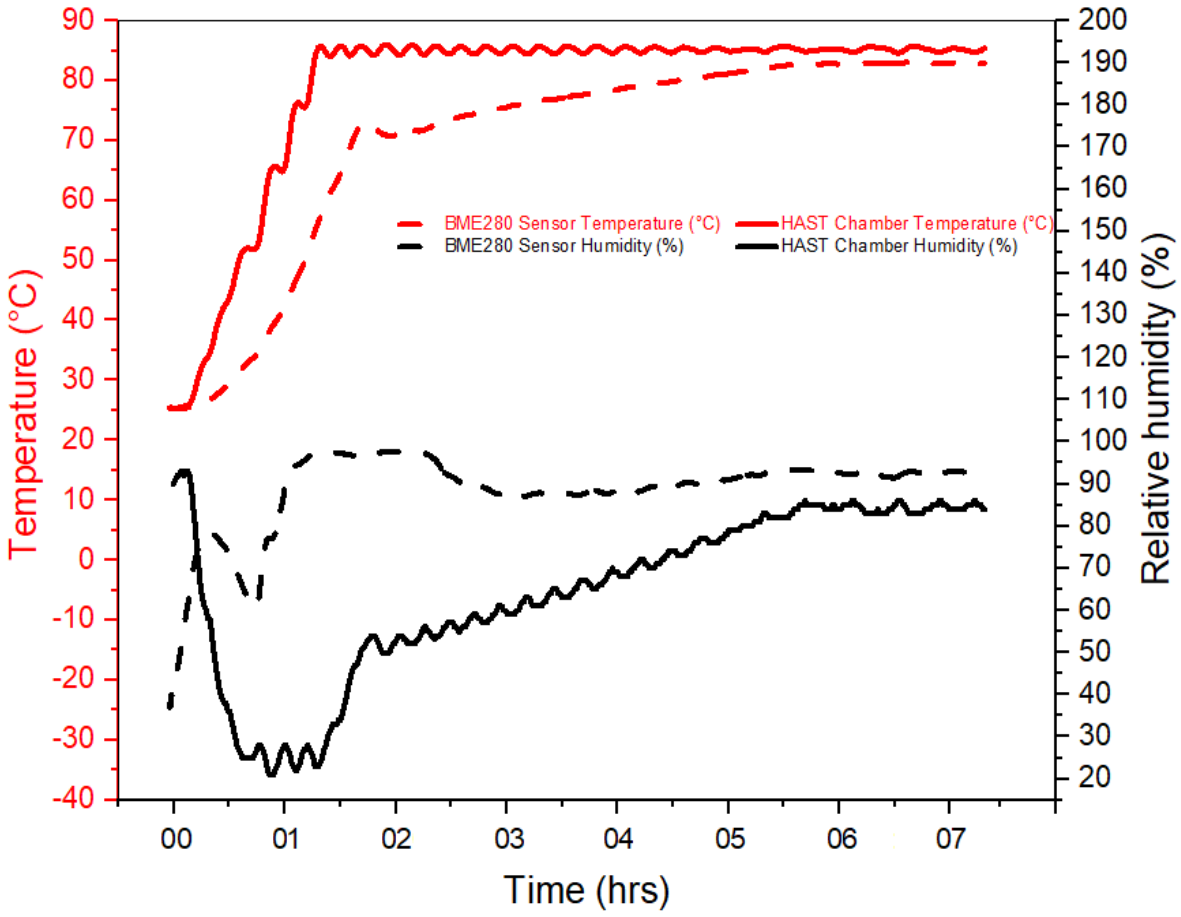

Figure 4.6: Comparison of temperature and humidity between BME280 reference sensor and HAST built-in sensors inside the chamber.

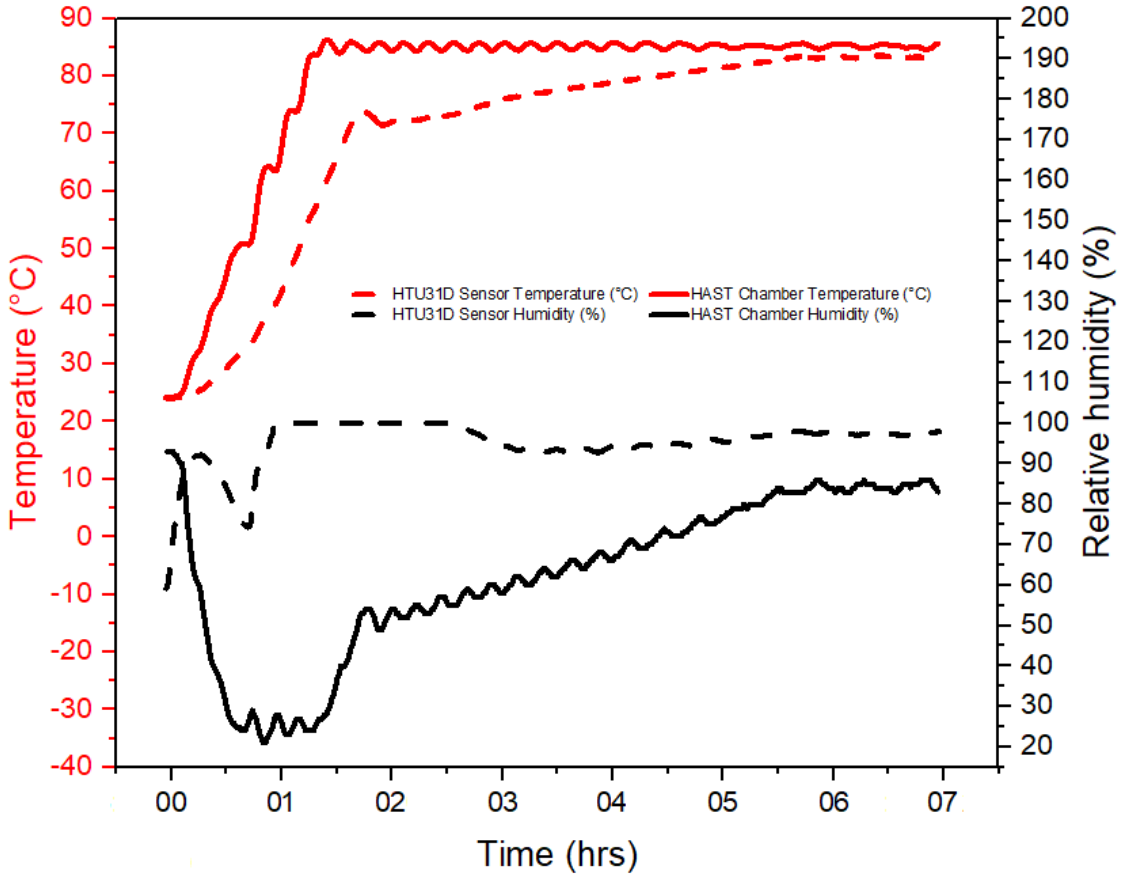

Figure 4.7: Comparison of temperature and humidity between HTU31D reference sensor and HAST built-in sensors inside the chamber.

Both reference sensors BME280 and HTU31D gave almost identical measurements of temperature and humidity inside the HAST chamber as can be seen in Figures 4.6 and 4.7. In terms of comparison with HAST built-in sensors, there was a large difference between the temperature measurements of both reference sensors and the HAST temperature sensor at the starting point, but after 6 hours the measurements stabilized and reached the set value of 85 °C with slight differences.

Initially, the humidity measurements of both reference sensors and HAST built-in sensors were contrary. The humidity of the HAST chamber was measured at over 100% RH by the reference sensors, whereas the humidity of the HAST chamber was measured up to 25% RH by the HAST sensors. But after 6 hours the measurements of both reference and HAST sensors were gradually stabilized towards the set value of 85 % inside the HAST chamber. But still, the reference sensors were measuring slightly above the set value. From these comparative measurements, a reference interval of up to 6 hours can be set for the characterization of EMFT temp-humidity sensors inside the HAST chamber. As the chamber required this period to stabilize and provide the desired temperature and humidity environment.

4.3 HAST chamber measurements

At last, the EMFT temperature-humidity sensors A and C with ceramic packages were inserted on Teflon-gold PCB and placed inside the HAST chamber to investigate the behavior of the humidity sensors. The chamber was operated in a constant mode where the relative humidity was set up to 85 % RH while the temperature was set at 130 °C. The test duration was 100 hours because this is a standard time period to test any electronic device inside the HAST chamber. Two power supplies were connected with each humidity sensor with an applied voltage of 30 V DC and the maximum current limit was 10 mA throughout the operation. After completion of the measurement within a specified period, the condition of the EMFT humidity sensors was observed under a microscope to determine whether any sensor was burnt or the layout had any structural damage during measurement. The microscopic images of EMFT temp-humidity sensors A and C can be seen in Figure 4.8.

Figure 4.8: Microscopic images of EMFT temperature-humidity sensors A and C after testing for up to 100 hours at 130 °C temperature with 85 % relative humidity inside the HAST chamber.

There was no damaged or burnt mark found on the layout of the humidity sensors. The bond wiring was also well connected, which indicated that both EMFT temp-humidity sensors could work in high temperature and humidity environments for a long duration, without any change in mechanical properties, and can also be reused for further measurements. However, the electrical properties of EMFT temp-humidity sensors could not be measured due to unnecessary leakage current found inside the HAST chamber and also the connections between the SMU power supplies and humidity sensors were unstable throughout the period. But the electrical characterizations of EMFT sensors could be possible in the future after debugging the leakage current inside the HAST chamber.

5. Summary and Outlook

5.1. Summary

At the end of this thesis, a quick summary of what was done and what results were obtained will be given.

A wafer probe analyzer was used to examine the electrical characteristics of EMFT temperature-humidity sensors A and C with a polyimide sensing layer at three different temperatures 25 °C, 85 °C, and 130 °C, in both AC and DC modesInitially, the capacitance of humidity sensors A and C was measured in a frequency range of 1 kHz to 1 MHz with an amplitude of 250 mV AC and a bias voltage of 30 V DC. Because of the change in impedance across the IDT electrodes, the capacitance of both sensors decreased with frequency. While the capacitance increased as temperature increased due to changes in the dielectric properties of the PI insulating material. The capacitance and conductance of EMFT humidity sensors were then measured at a constant frequency of 1 kHz with biases ranging from -30 V to +30 V DC in 0.3 V steps. The capacitance and conductance increased with increasing temperature but remained unchanged throughout the test. The current was measured in EMFT humidity and temperature sensors A and C, with a current limit of 10mA and biases ranging from 0 V to 30 V in 0.1 mV and 10 mV steps. Because of the ionization of charges between IDT electrodes, the conductance of humidity sensors increased while the resistance decreased with temperature. However, the vibration of gold atoms increased resistance and decreased conductance in temperature sensors. Furthermore, the bidirectional resistance of both temperature sensors A and C were tested at six different temperatures within the same range of 25 °C to 130 °C with a current limit of 5mA. As the temperature increased, the resistance of both sensors increased. Similarly, when the temperature decreased, the resistance of both temperature sensors also decreased. The temperature and humidity within the HAST chamber were simultaneously measured in the next phase of the measurements. Temperature and humidity measurements from each reference humidity sensor BME280 and HTU31D were compared to measurements from HAST built-in sensors. The HAST chamber was run in a constant mode for 8 hours at 85 °C with a humidity set value of 85% RH. Based on

these comparison data, a reference interval of up to 6 hours for the characterization of EMFT temperature-humidity sensors inside the HAST chamber could be defined. This interval was required since the chamber needed to settle and provide the desired temperature and humidity conditions.
The chamber was run in a continuous mode with the relative humidity set at 85% RH and the temperature set to 130 °C. The testing duration was 100 hours. Throughout the operation, two power supplies were connected to each humidity sensor, with an applied voltage of 30 V DC and a maximum current restriction of 10 mA. There were no damaged or burned marks on the humidity sensor layout. The bond wire was also firmly connected, indicating that both EMFT temperature-humidity sensors could operate in high temperature and humidity conditions for an extended period of time without change in mechanical properties and may be reused for future measurements. However, due to the excessive leakage current observed within the HAST chamber, the electrical characteristics of the EMFT temp-humidity sensors could not be monitored, and the connections between the SMU power supply and humidity sensors were unstable during the duration.

5.3 Outlook

Throughout the period, EMFT temperature-humidity sensors A and C gave sufficient results of electrical measurements on the wafer probe analyzer in both AC & DC Modes. However, further measurements could still be possible by changing the frequency ranges to see the capacitive behavior of both sensors. The resistive responses of temperature sensors can be examined at below 25 °C or above 130 °C.
A comparison of the temperature and RH values between the two reference sensors and the HAST built-in sensors provides information for setting a reference interval of up to 6 hours for testing the EMFT sensor inside the HAST chambers. But this reference period was set only for 85 °C and 85 % RH. Another comparative measurement at 125 °C temperature and 100 % RH could be possible with the HTU31D reference sensor. If a schematic layout can be fabricated on Teflon-gold PCB.
The HAST system still needs to be better understood. The resistive measurements of EMFT sensors with ceramic packages should be examined inside the HAST chamber at 130 °C and 85% RH, to determine if any failure inside the sensors during operation. The system itself runs very smoothly but the reliability of the SMU should be improved and if necessary, another way to provide voltage and measure the current has to be found.

Bibliography

1. Barmpakos, D. and G. Kaltsas, *A review on humidity, temperature and strain printed sensors—current trends and future perspectives.* Sensors, 2021. **21**(3): p. 739.
2. Wei, P., et al., *Impact analysis of temperature and humidity conditions on electrochemical sensor response in ambient air quality monitoring.* Sensors, 2018. **18**(2): p. 59.
3. Grasley, Z.C., et al., *Relative humidity in concrete.* Concrete international, 2006. **28**(10): p. 51-57.
4. Venkat, N., et al., *High-temperature polymer film dielectrics for aerospace power conditioning capacitor applications.* Materials Science and Engineering: B, 2010. **168**(1-3): p. 16-21.
5. Krivec, T., *Reliability Performance of Very Thin Printed Circuit Boards with regard to Different any-Layer Manufacturing Technologies.*
6. Michalski, S., *Relative humidity: a discussion of correct/incorrect values.* mh, 1993. **500**(3): p. 1oo.
7. Lawrence, M.G., *The relationship between relative humidity and the dewpoint temperature in moist air: A simple conversion and applications.* Bulletin of the American Meteorological Society, 2005. **86**(2): p. 225-234.
8. Nguyen, J.L., J. Schwartz, and D.W. Dockery, *The relationship between indoor and outdoor temperature, apparent temperature, relative humidity, and absolute humidity.* Indoor air, 2014. **24**(1): p. 103-112.
9. Gatley, D.P., *Psychrometric chart celebrates 100th anniversary.* ASHRAE Journal, 2004. **46**(11): p. 16.
10. Lee, C.-Y., et al. *Microcantilever-based Weather Station for Temperature, Humidity And Wind Velocity Measurement*. in *DTIP 2007*. 2007. TIMA Editions.
11. Park, S.Y., et al., *Room temperature humidity sensors based on rGO/MoS2 hybrid composites synthesized by hydrothermal method.* Sensors and Actuators B: Chemical, 2018. **258**: p. 775-782.
12. Blasch, K.W., et al., *New field method to determine streamflow timing using electrical resistance sensors.* Vadose Zone Journal, 2002. **1**(2): p. 289-299.
13. Bentley, J., *Temperature sensor characteristics and measurement system design.* Journal of Physics E: Scientific Instruments, 1984. **17**(6): p. 430.
14. Zhao, R., et al., *Temperature sensor made of polymer-derived ceramics for high-temperature applications.* Sensors and Actuators A: Physical, 2014. **219**: p. 58-64.
15. Reverter, F. and O. Casas, *Direct interface circuit for capacitive humidity sensors.* Sensors and Actuators A: Physical, 2008. **143**(2): p. 315-322.

16. Boudaden, J., et al., *Polyimide-based capacitive humidity sensor.* Sensors, 2018. **18**(5): p. 1516.
17. Kim, J.-H., et al. *High sensitivity capacitive humidity sensor with a novel polyimide design fabricated by MEMS technology*. in *2009 4th IEEE International Conference on Nano/Micro Engineered and Molecular Systems*. 2009. IEEE.
18. ChitraP, L., *COMPARATIVE ANALYSIS OF CANTILEVER TYPE MEMS DEVICE FOR HUMIDITY MEASUREMENT.*
19. Hong, E., et al., *Micromachined piezoelectric diaphragms actuated by ring shaped interdigitated transducer electrodes.* Sensors and Actuators A: Physical, 2005. **119**(2): p. 521-527.
20. Mengerink, Y., et al., *Separation and quantification of the linear and cyclic structures of polyamide-6 at the critical point of adsorption.* Journal of Chromatography A, 2001. **914**(1-2): p. 131-145.
21. Ha, C.-S. and A.S. Mathews, *Polyimides and high-performance organic polymers*, in *Advanced Functional Materials*. 2011, Springer. p. 1-36.
22. Deligöz, H., et al., *Electrical properties of conventional polyimide films: effects of a chemical structure and water uptake.* Journal of applied polymer science, 2006. **100**(1): p. 810-818.
23. Ko, Y.-G., et al., *Various digital memory behaviors of functional aromatic polyimides based on electron donor and acceptor substituted triphenylamines.* Macromolecules, 2012. **45**(9): p. 3749-3758.
24. Goshi, N., et al., *Glassy carbon MEMS for novel origami-styled 3D integrated intracortical and epicortical neural probes.* Journal of Micromechanics and Microengineering, 2018. **28**(6): p. 065009.
25. Jameson, N.J., M.H. Azarian, and M. Pecht. *Thermal degradation of polyimide insulation and its effect on electromagnetic coil impedance*. in *Proceedings of the Society for Machinery Failure Prevention Technology 2017 Annual Conference*. 2017.
26. Dakin, T., *Conduction and polarization mechanisms and trends in dielectric.* IEEE Electrical Insulation Magazine, 2006. **22**(5): p. 11-28.
27. Jia, C., et al., *Bond electronic polarization induced by spin.* Physical Review B, 2006. **74**(22): p. 224444.
28. Kirkwood, J.G., *On the theory of dielectric polarization.* The Journal of Chemical Physics, 1936. **4**(9): p. 592-601.
29. Sundar, V. and R. Newnham, *Electrostriction and polarization mechanism.* Ferroelectrics, 1992. **135**(1): p. 431-446.
30. Kajtoch, C., *Dipolar polarization in Ba (Ti1− xSnx) O3.* Ferroelectrics, 1995. **172**(1): p. 465-468.
31. Izgorodina, E.I., M. Forsyth, and D.R. MacFarlane, *On the components of the dielectric constants of ionic liquids: ionic polarization?* Physical chemistry chemical physics, 2009. **11**(14): p. 2452-2458.
32. Macdonald, J.R., *Theory of ac space-charge polarization effects in photoconductors, semiconductors, and electrolytes.* Physical Review, 1953. **92**(1): p. 4.
33. Lima, M., et al., *Structural, electrical and thermal properties of borosilicate glass–alumina composites.* Journal of Alloys and Compounds, 2012. **538**: p. 66-72.

34. Bockelman, D.E. and W.R. Eisenstadt, *Pure-mode network analyzer for on-wafer measurements of mixed-mode S-parameters of different circuits.* IEEE Transactions on Microwave Theory and Techniques, 1997. **45**(7): p. 1071-1077.
35. Yamamoto, T., *Humidity Measurement and Control in the HAST.* ESPEC Technology Report, No. 5, 1998: p. 11-19.
36. Yamamoto, T., *Humidity Measurement and Control by BME280 circuit board.* ESPEC Technology Report, No. 5, 1998: p. 11-19.
37. Chharia, A., et al. *NeT-vent: low-cost, rapidly scalable and IoT-enabled smart invasive mechanical ventilator with adaptive control to reduce incidences of pulmonary barotrauma in SARS-CoV-2 patients*. in *2021 2nd global conference for advancement in technology (GCAT)*. 2021. IEEE.
38. Olajire, O.T., *An analysis of pressure, temperature, and humidity in a room using a Raspberry pi/Arduino uno/Arduino uno and BME280*. 2020, Dublin, National College of Ireland.
39. Hamblen, J.O. and G.M. Van Bekkum, *An embedded systems laboratory to support rapid prototyping of robotics and the internet of things.* IEEE Transactions on Education, 2012. **56**(1): p. 121-128.
40. Sensor, A.L.A.I.C., *HTU31D Breakout Board*. 2018.
41. BME280 Sensor, P., *Breakout board.* Available at SSRN 4096563.
42. Santos, R. and S. Santos, *Arduino Uno pin connections with Humidity Sensors.* Random Nerd, 2018.
43. Kennelly, A.E., *Impedance.* Transactions of the American Institute of Electrical Engineers, 1893. **10**: p. 172-232.
44. Geis, M., J. Gregory, and B. Pate, *Capacitance-voltage measurements on metal-SiO/sub-2/-diamond structures fabricated with.* IEEE transactions on electron devices, 1991. **38**(3): p. 619-626.
45. Spray, D., A. Harris, and M. Bennett, *Equilibrium properties of a voltage-dependent junctional conductance.* The Journal of general physiology, 1981. **77**(1): p. 77-93.
46. Sorensen, J.A. and G.E. Glass, *Ion and temperature dependence of electrical conductance for natural material.* Analytical Chemistry, 1987. **59**(13): p. 1594-1597.
47. Safi, I., C. Bena, and A. Crépieux, *Ac conductance and nonsymmetrized noise at a finite frequency in quantum wires and carbon nanotubes.* Physical Review B, 2008. **78**(20): p. 205422.
48. Elhadidy, H., J. Sikula, and J. Franc, *Symmetrical current-voltage characteristic of a metal-semiconductor-metal structure of Schottky contacts and parameter retrieval of a CdTe structure.* Semiconductor science and technology, 2011. **27**(1): p. 015006.
49. Fors, R., S.I. Khartsev, and A.M. Grishin, *Resistance switching in metal-insulator-manganite junctions: Evidence for Mott transition.* Physical Review B, 2005. **71**(4): p. 045305.
50. De Haas, W., J. De Boer, and G. Van den Berg, *The electrical resistance of gold, copper, and lead at high temperatures.* Physica, 1934. **1**(7-12): p. 1115-1124.
51. Gold, A. and V. Dolgopolov, *Temperature dependence of the conductivity for gold metal.* Physical Review B, 1986. **33**(2): p. 1076.

Appendix

a. Arduino coding for BME280 sensor

```
#include <Wire.h>
#include <Adafruit_Sensor.h>
#include <Adafruit_BME280.h>
Adafruit_BME280 bme;
void setup() {
  Serial.begin(9600);
  if (!bme.begin(0x76)) {
    Serial.println("Could not find a valid BME280 sensor, check to wire!");
    while (1);
      }
      else {
        Serial.print("BME-Temperature [°C], Humidity [%r.H.]");
        delay(2000);
        Serial.println();
      }
   }
void loop() {

        Serial.print(bme.readTemperature());
        Serial.print(" ");
        Serial.print(bme.readHumidity());
        Serial.println();
        delay(5000);

  }
```

Fig. A: Arduino Uno microcontroller coding for BME280 reference sensor.

b. Arduino coding for HTU31D sensor

```
#include <Wire.h>
#include <Adafruit_HTU31D.h>
Adafruit_HTU31D htu = Adafruit_HTU31D();
void setup() {
  Serial.begin(9600);
  if (!htu.begin(0x40)) {
    Serial.println("Could not find a valid HTU31D sensor, check to wire!");
    while (1);
     }
     else {
       Serial.print("HTU-Temperature(*C), Humidity(%)");
       Serial.println();
     }
   }
void loop() {
     sensors_event_t humidity, temp;
     htu.getEvent(&humidity, &temp);
       Serial.print(temp.temperature);
       Serial.print(" ");
       Serial.print(humidity.relative_humidity);
       Serial.println();
       delay(10000);
  }
```

Fig. B: Arduino Uno microcontroller coding for HTU31D reference sensor.

Declaration of Authorship

I **Syed Fahad Ali,** Matriculation nr: **03091019** declare that the submitted work has been completed by me the undersigned and that I have not used any other than permitted reference sources or materials nor engaged in any plagiarism. All references and other sources used by me have been appropriately acknowledged in the work.

I further declare that the work has not been submitted anywhere else for academic examination, either in its original or similar form.

Munich, 01.09.2022

_____

(Syed Fahad Ali)